Semi-autonomous robotic control of a self-shaping cochlear implant

Daniel Bautista-Salinas[1,2], Conor Kirby[1,2], Mohamed E. M. K. Abdelaziz[1], Burak Temelkuran[3],
Charlie T. Huins[4] and Ferdinando Rodriguez y Baena[1,2], *Member, IEEE*

Abstract— Cochlear implants (CIs) can improve hearing in patients suffering from sensorineural hearing loss via an electrode array (EA) carefully inserted in the scala tympani. Current EAs can cause trauma during insertion, threatening hearing preservation; hence we proposed a pre-curved thermally drawn EA that curls into the cochlea under the influence of body temperature. However, the additional surgical skill required to insert pre-curved EAs usually produces worse surgical outcomes. Medical robots can offer an effective solution to assist surgeons in improving surgical outcomes and reducing outliers. This work proposes a collaborative approach to insert our EA where manageable tasks are automated using a vision-based system. The insertion strategy presented allowed us to insert our EA successfully. The feasibility study showed that we can insert EAs following the defined control strategy while keeping the exerted contact forces within safe levels. The teleoperated robotic system and robotic vision approach to control a self-shaping CI has thus shown potential to provide the tools for a more delicate and atraumatic approach.

I. INTRODUCTION

A cochlear implant (CI) is currently the most effective treatment for sensorineural hearing loss. It works by converting sound into electrical pulses sent through an electrode array (EA) to the cochlea. The EAs found in commercial CIs can be distinguished depending on their final position within the cochlea. A lateral wall EA (LEA) sits close to the outer or lateral wall of the scala tympani (ST, a helical chamber of the cochlea where the EA is inserted), and a perimodiolar EA (PEA) sits close to the inner or modiolar wall of the ST.

A LEA is a very thin and flexible EA often inserted through the round window (RW), a natural opening of the cochlea created after pealing the RW membrane. Since it is a straight EA, it must contact the ST walls during insertion to curls into the ST spiral. These contacts can generate intracochlear trauma, according to research conducted by a CI company (Cochlear Ltd., Australia [1]). Intracochlear trauma can lead to residual hearing loss [2], which is essential to preserve in order to enhance the patient´s hearing outcomes [3]. The LEA position, far from the hearing cells located in the modiolar wall, results in lower stimulation efficiency and performance [4]. These disadvantages can be overcome using a PEA, a pre-curved EA which sits close to the modiolar wall. It uses a mechanism that allows the EA to have a straight shape outside the cochlea and, as it is inserted, recover its initial shape. The CI512 Contour Advance PEA (Cochlear Ltd.) shaping mechanism consists of an inner stylet removed during insertion to allow the EA to curl into the ST. This type of insertion reduces contact forces and enhances hearing outcomes [4]. However, the stylet increases the EA diameter and, as a result, the EA cannot be inserted through the RW, requiring a cochleostomy (i.e., drilling procedure to create a wider opening), a process which contributes to early translocation from the ST to the scala vestibuli (SV) [5].

The CI532 Slim Modiolar (Cochlear Ltd., Australia) is a PEA developed to overcome this problem. It uses a $0.68\ mm$ diameter sheath inserted $5.5\ mm$ into the ST to guide the EA until the first turn and allow curling from this point. The soft material of its sheath makes a RW insertion possible. Nevertheless, data is limited, and using a physical shaping mechanism increases the procedure risk [1]. To solve this problem, H. Ajieren *et al.* [6] introduced a pre-curved EA that does not rely on a physical shaping mechanism. They used a shape memory polymer (SMP) to develop an EA, which can stay straight at room temperature and curl when in contact with the body temperature. To fabricate such EA, we proposed using thermal fibre drawing [7]. This process can create very thin and long SMP fibres that we cut to the appropriate dimensions and mould into the ST shape. The initial evaluation of this pre-curved EA showed that the forces generated upon recovery were below the rupture threshold (i.e., the limit that causes trauma [1]).

These recovery forces are one of the factors that can cause trauma. Another inherent problem of PEAs is the additional surgical skill required to insert them, which results in worse surgical outcomes [8]. Medical robots can offer an effective solution to assist surgeons in improving surgical outcomes and reducing outliers. There have been different attempts to develop robotic assistance devices and autonomous robots to control the insertion of both LEAs [9] and PEAs [10], [11]. To assist during the insertion of our SMP-based PEA, we propose a collaborative robot with a level of autonomy in line with medical robots regulations and commercial approaches [12], where more manageable tasks are automated, and the surgeon supervises and controls the rest of the procedure. The robot will be used to study the feasibility of successfully inserting our self-shaping EA semi-autonomously and to assess, in a relevant setup, if the forces exerted during insertion are below the rupture threshold.

II. Self-Shaping Electrode Array

A thermally responsive shape memory polymer (SMP) can recover its original shape from a temporary one, achieved after deformation and fixation, when it is under an external temperature stimulus (e.g. body temperature). To fabricate the self-shaping EA, we started from SMP pellets (SMP Technologies Inc., Japan) to create a cylindrical preform with the final device cross-section. This cross-section has an inner lumen that can be used for sensing and therapeutics, such as the corticosteroids used in clinical practice. The preform was used to obtain the desired EA diameter filaments, approximately $1.5\ mm$, following a thermal drawing process; filaments were then moulded into the 2D shape of a 3x scaled-up version of the ST. Each EA was moulded at $80°C$ for $15\ min$, using a CNC machined Teflon mould (Proto Labs Ltd., UK). After cooling, the EA was attached to a frictional fixture used to connect the EA to the robot (Fig. 1). Then, the EA was programmed into a straight shape. For this, we warmed it up by placing it in water slightly above its transition temperature ($35°C$) for $30\ s$. Immediately after, the EA was placed in a $4°C$ bath for another $30\ s$ to fix its temporary position. The dummy EAs used in this work were not fabricated with electrodes, with a more detailed description of the self-shaping EA found in [7].

III. Robotic System

A. Design and Actuation

In conventional CI surgery, the surgeon inserts the EA delicately and dexterously into the ST. The EA insertion approach angle to the ST and the insertion velocity are critical to reducing intracochlear trauma and preserving residual hearing [13], [14]. Then, a CI surgery robotic system has to achieve accurate linear motion and allow angular movements to adjust the approach angle. Additionally, to avoid touching the ST walls and translocation into the SV and the associated intracochlear trauma, the robot should be able to modify the angle around the EA axis. Lastly, the system must be compact to be used in a operating theatre without disrupting the current workflow. To address these requirements, we developed a 4 degrees of freedom teleoperated robot.

The robot presents a modular design. The first module, which can adjust the height and approach angle, was used to align the EA with respect to the ST model. The second module controlled the insertion parameters: linear motion and EA roll angle. This design allowed the evaluation of our EA in an experimental setting. Additionally, it was designed for rapid integration in the operating theatre since the insertion module can be mounted onto a robotic arm that would replace the alignment module and provide the manoeuvrability needed in surgery. Since the insertion was planar in our experiments, the height was adjusted manually initially, and we did not change it throughout the experiments.

The linear insertion motion was achieved with a lead screw actuated with a brushless DC-Servomotor (2057S 024B K1155, Faulhaber, Germany). This motor can operate at speeds lower than the ones used in manual insertions to
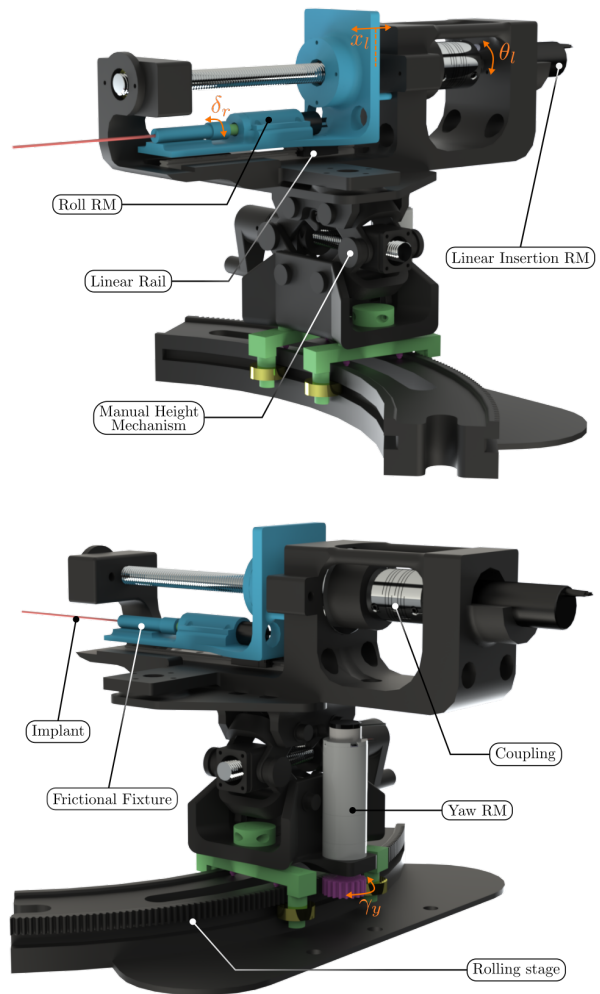

Fig. 1. CAD renderings of the proposed robot. RM: rotary motor.

minimise intracochlear trauma, which are close to $1\ mm/s$ [15], and it uses analogue hall sensors, which provided a lightweight and compact alternative to encoders. The insertion unit, where the EA was loaded, was attached to the lead screw and sat on a linear slider (Misumi, Germany) that acted as a rail and minimised friction, yielding a stroke length of $77\ mm$. The insertion unit had a brushless DC-Servomotor with analogue hall sensors (1226A 012B K1855, Faulhaber, Germany) combined with a planetary gearhead with a reduction ratio of 16:1 (12/4, Faulhaber, Germany). This allowed for accurate control of the roll.

A frictional fixture was pressed fit into the motor shaft to load the EAs rapidly. Quick loading is essential to minimise procedure times. It was also necessary since we did not have a device to maintain the EA temperature below the shape-changing threshold to keep the EA straight while loading and advancing from the RW to the first turn - hence the need to begin the insertion a few seconds after the EA was removed from the refrigerated chamber. The yaw motion was actuated via a custom brushless DC-Servomotor with analogue hall sensors (Maxon Group, Switzerland), used to
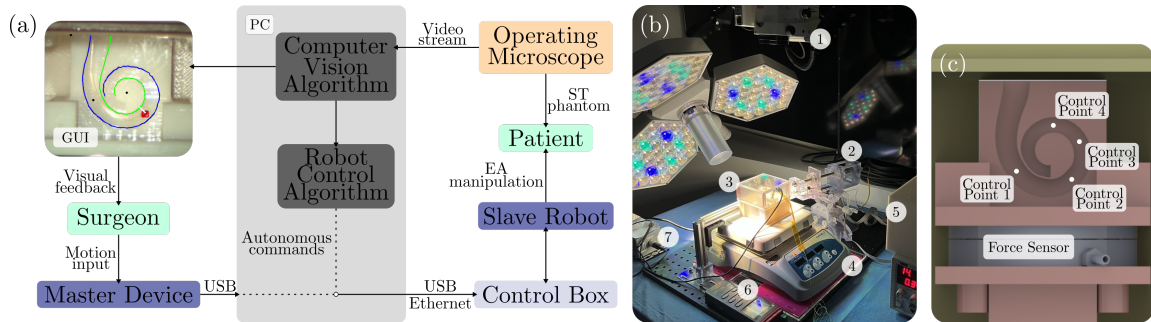
Fig. 2. (a) Control architecture and (b) experimental setup, where (1) Operating microscope, (2) Slave robot, (3) Scala tympani (ST) phantom, (4) Hot plate, (5) Power supply and control box, (6) Temperature reader, (7) Force sensor reader. (c) ST and force sensor close-up, with the control points overlaid.

control the insertion approach angle. The robot parts were printed with an Object 500 (Stratasys, USA) using VeroClear and VeroWhite materials (standard quality, glossy finish), allowing rapid prototyping and lightweight parts. Renderings of the robot are shown in Fig. 1.

B. Control Scheme

A hybrid-control approach was followed to insert the EA. The linear motion was automated to compensate for the EA shape changes swiftly and safely, while roll and yaw were controlled manually. The linear insertion control mode could be switched from automatic to manual, providing the user complete control over the procedure. The motor controllers were programmed in C++ on a Linux PC. The linear motion was velocity-controlled to maintain safe speeds with an EtherCAT controller (MC 5004 P STO, Faulhaber, Germany). A proportional closed-loop controller was implemented to drive the EA insertion. The algorithm adjusted the insertion velocity based on the current distance of the EA tip to the modiolar wall, which was calculated with an automated vision-based algorithm. The insertion velocity was described as:

$$v_i(t) = k_c \cdot (SP - d_M(t)) \tag{1}$$

where k_c is the system proportional gain, SP is the setpoint or desired distance to the modiolar wall, and $d_M(t)$ is the current distance to the modiolar wall. Live images from an operating microscope (Leica M525 OH4, Leica Microsystems Ltd., UK) placed roughly perpendicular to the phantom were acquired with an AJA HA5-Plus converter (AJA Video Systems Inc., California, USA) linked to an AJA Kona 4 PCIe framegrabber. Using one of these images, the user drew the ST walls contours. Then, using colour segmentation, the EA tip was detected, and the distance to the modiolar wall was calculated and used as an input into the system.

The user controlled the procedure through a GUI displayed on a separate screen. The GUI showed a live feed from the microscope over which some features were overlaid. These features included the point in the EA tip detected, a line showing the distance from the EA tip to the modiolar wall measured, and the ST walls contours. Processing of these images was done using the OpenCV library in C++ [16]. This GUI also allowed the user to decide if it was necessary to

intervene and control the linear insertion and to decide if yaw and roll angles needed to be adjusted. The roll, controlled with another EtherCAT controller, and yaw, with a serial EPOS2 Module 36/2, were position-controlled to achieve the desired angles. Teleoperation was performed in a master-slave configuration with a keyboard controller as the master device. A flow diagram of the control architecture is shown in Fig. 2a.

IV. EXPERIMENTS

A. Shaping Rate Study

The insertion of commercial pre-curved EAs using stylet- and sheath-based shaping mechanisms follow the standardised AOS trajectory. In this technique, the EA is kept straight until the first turn, and then, the EA starts curling progressively into the ST. The EA tip is kept close to the modiolar wall to maximise the insertion depth angle while avoiding contact with the ST walls and translocation into the SV. To allow our EA to follow this progressive insertion technique, we must map the curling velocity, v_c, to the robot insertion velocity, v_i. Due to variability in the fabrication and moulding processes, the curling velocity is unknown and difficult to characterise. To tackle this, we defined four control points (CPs) along the ST at the locations where direction changes occur (Fig. 2c). The insertion trajectory was set at the ST centreline to allow room for curling.

The controller velocity limit was initially set to 2 mm/s. We evaluated this control strategy. Then, we followed an iterative process to tune the controller velocity limits for each section delimited by adjacent CPs until $v_i \approx v_c$. In each test, the insertion unit travelled until the end of the linear rail, and then we waited for 5 s to allow for the final shape changes. To assess these control strategies, we recorded from CP 1 distance to the modiolar wall, insertion velocity and the insertion depth angle. The insertion depth angle is considered successful for values between 330° and 390° [17]. An example of the depth angle measurement is shown in Fig. 6k.

The experiments were conducted in an unlubricated 3x scaled-up planar model of the ST adapted from an open-source design [18]. A lubricated ST can yield more realistic force values; however, we decided to conduct our experiments using an unlubricated ST to report the worst scenario

for insertion contact forces. The ST phantom was enclosed in a chamber, and the assembly was placed over a hotplate (VWR International, USA) to simulate the body temperature inside the enclosure (Fig. 2b-c). The GUI was used to visualise and assess the insertion process in this setup. Before insertion, the EA was kept at $5°C$, and after loading it into the robot, the user started the insertion immediately. After that, linear insertion was controlled autonomously, and the user modified the rotation and approach angle when needed.

The first control strategy resulted in a successful insertion of 370°. In this test, the EA tip reached the midpoint between CP 2 and 3 without contacting the ST walls. After this point, the insertion velocity started to be significantly lower than the curling velocity, causing the EA tip to approach the modiolar wall. The controller velocity limit was too low to compensate for this, and it could not move the EA further into the ST to recover the desired trajectory line. The tip contacted the modiolar wall after CP 3, and the friction made the EA start buckling until the EA contacted the lateral wall. The friction with the lateral wall allowed the insertion to continue.

To overcome the problems with the previous strategy, we increased the velocity limit to $5\ mm/s$ between CP 1 and 2. This strategy also reached a successful depth of 373°. The changes introduced here allowed the EA tip to reach CP 3 without contacting the ST walls. After the tip passed CP 2, the middle part of the EA was quite close to the modiolar wall, but it did not contact it. However, just after CP 3, the insertion velocity started to be lower than the curling velocity, which led to the same buckling effect observed in the first control strategy. Again, the friction with the lateral wall allowed the insertion to continue. We also noticed that after CP 4, the position of the tip was very close to the modiolar wall, whilst between CP 1 and 2, the EA was in a middle position in the ST.

In the following iteration, we kept the velocity limit at $5\ mm/s$ until CP 3 and increased it to $3\ mm/s$ from CP 3 onwards. The higher velocity limit after CP 3 avoided buckling since the insertion velocity was similar to the curling velocity. However, the EA contacted the lateral wall when the tip was at a depth of 220°. Although this is not ideal, contacting the lateral wall is preferred as it leads to less trauma since hearing cells are closer to the modiolar wall. Moreover, after CP 4, we changed the k_c sign to force the robot to retract the EA. This change slightly separated the tip from the modiolar wall while placing the EA in a perimodiolar position in the region delimited by CP 1 and 2. The insertion depth was also successful, 354°.

This evaluation shows that the CPs defined here can be used to map the curling velocity to the insertion velocity and avoid contact with the modiolar wall using a pre-planned insertion trajectory. The velocity values, however, have to be treated as a guide. Variability in the fabrication and moulding processes affects the curling rate (i.e., the curling velocity) and behaviour (i.e., trajectory), which explains the differences following the insertion trajectory and insertion depth. For all three control strategies, it can be observed in Fig. 3 that the EA does not start from the desired trajectory
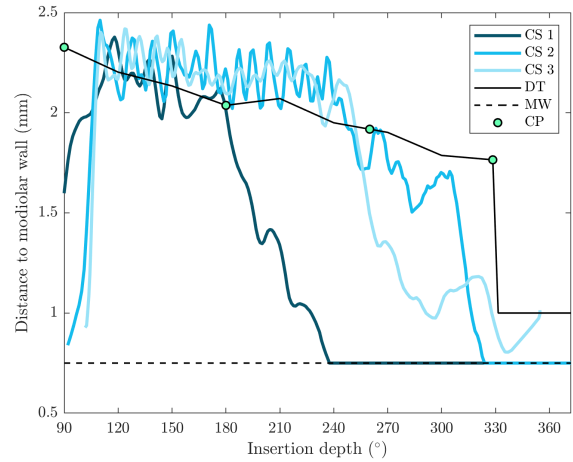

Fig. 3. Plot showing the EA tip distance to the modiolar wall during insertion for the different control strategies tested. CS: control strategy. DT: desired trajectory. MW: modiolar wall. CP: control point.
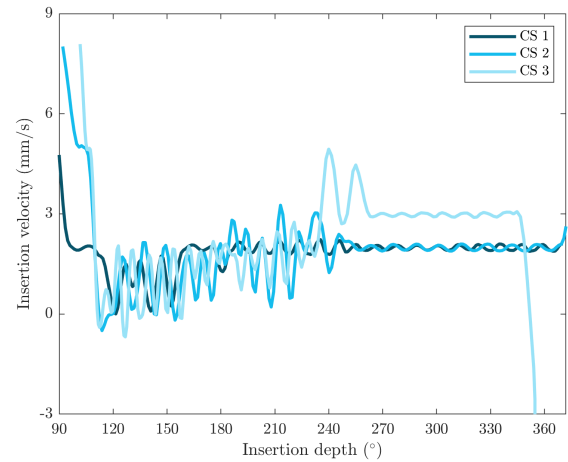

Fig. 4. Plot showing the EA velocity during insertion for the different control strategies tested. CS: control strategy.

since it has already started to recover shape. We also noted that the insertion velocity was high for atraumatic insertions, especially at CP 1 and a few degrees after. The insertion velocity could be reduced by controlling the EA temperature while loading it onto the robot and during insertion. This could be achieved by creating temporary hypothermia ($31°C$) [19] to prevent shape changes which quickly happen when the EA is heated above $32°C$ [7].

The velocity plot (Fig. 4) shows how the higher velocity limit in control strategies 2 and 3 after CP 1 made the EA overshoot the desired trajectory, which led to the tip overcoming the first corners without contacting the modiolar wall. This result suggests that the desired trajectory might need to be pushed back further from the modiolar wall between CP 1 and 2. We also observed contacts with the lateral wall even for the optimal case (control strategy 3) after CP 2, which could be caused by our trajectory being further from the modiolar wall than the AOS trajectory. Additionally, the

	Insertion 1	Insertion 2	Insertion 3	Insertion 4	Insertion 5	Insertion 6
Insertion depth angle (°)	345.51	352.42	385.71	376.26	390.06	368.16
Insertion velocity (mm/s)	0.78 ± 1.46	0.62 ± 1.52	2.22 ± 1.22	0.31 ± 1.02	0.97 ± 1.83	0.70 ± 1.38
Approach angle (°)	6.04 ± 0.65	9.01 ± 3.70	17.45 ± 5.02	9.18 ± 2.45	8.15 ± 0.97	14.19 ± 1.30
Roll angle (°)	79.13 ± 15.19	-203.31 ± 24.00	-0.01 ± 0.01	28.12 ± 4.19	28.20 ± 7.72	73.44 ± 20.10
	Insertion 7	**Insertion 8**	**Insertion 9**	**Insertion 10**	**Insertion 11**	
Insertion depth angle (°)	356.80	353.74	346.37	348.78	352.12	
Insertion velocity (mm/s)	0.27 ± 0.96	0.78 ± 1.61	0.98 ± 1.83	1.01 ± 1.92	0.89 ± 1.89	
Approach angle (°)	9.97 ± 1.09	8.90 ± 0.86	11.46 ± 0.28	5.93 ± 0.31	10.12 ± 1.57	
Roll angle (°)	19.77 ± 2.07	84.93 ± 18.47	25.76 ± 4.43	73.49 ± 14.56	26.40 ± 5.67	

Insertion velocity, approach angle and roll angle represent the mean and standard deviation from the control point 1.

buckling effect may be reduced in a real lubricated cochlea. Nevertheless, results show that the strategy described here has the potential to minimise contact with the modiolar wall. Further work will focus on studying different insertion trajectories that can reduce contacts with the lateral wall without compromising the modiolar wall.

B. Insertion Feasibility Evaluation

The findings in IV-A show that control strategy 3 was preferable. However, the velocity limit between CP 2 and 3 of 5 mm/s did not seem to provide any advantage over the 2 mm/s used in control strategy 2. Therefore, this change was reverted. To study the repeatability of this strategy and assess the contact forces exerted during insertion, we tested fifteen EAs. To measure insertion forces in the Z-direction, we added a 6-axis force/torque sensor (Nano43, ATI Industrial Automation, USA) to the back of the ST phantom (Fig. 2c). We measured the depth angle and Z-direction force to evaluate the insertions. Forces were negative in the insertion direction. Motor values and vision data were also recorded. Samples were inserted, and then we waited for 10 s after the robot motion had been completed to stop recording data. Due to failure of the force sensor attachment, the first four samples were discarded from the analysis. The insertion depth was successful for all tested samples, ranging from 345.51° to 390.06°. Tip fold-over was not observed during any of the insertions. The rupture threshold forces are usually above 120 mN, but sometimes they can be as low as 40 mN [1]. In our case, seven of the eleven insertions recorded peak forces beyond 40 mN, and only one insertion overcame the 120 mN barrier, reaching 226.33 mN between the RW and CP 1. In Table I, the main results for all the insertions are summarised. In Fig. 5, the force distribution and mean for each test from CP 1 is shown.

A detailed force profile and screenshots of key moments for representative insertions six and nine are shown in Fig. 6. In both insertions, a peak force was recorded before the insertion. This peak force was generated during EA loading. In the insertion nine profile, it can be appreciated that forces started becoming negative after loading as the tip pressed against the modiolar wall in the insertion direction (Fig. 6h). As the insertion progressed, the pressure into the modiolar
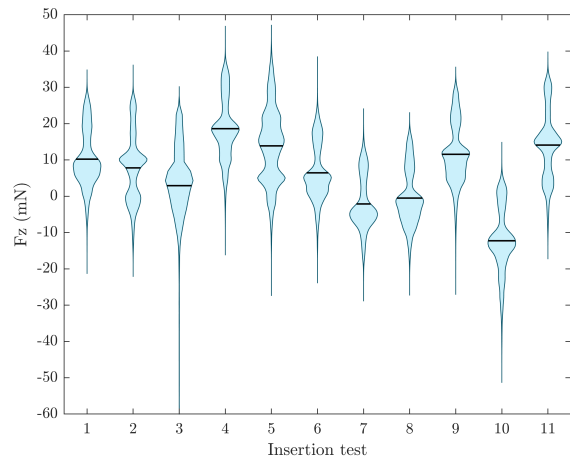

Fig. 5. Violin plot showing the force distribution for the eleven tests conducted. The horizontal blue line for each test represents the mean force. In test 3 the lower end reached -226.936 mN.

wall decreased, and forces started recovering to the baseline of 0 mN (Fig. 6i). Then, the body contacted the lateral wall in the insertion direction, and the forces started to decrease again (Fig. 6j). After CP 3, the robot compensated for this, and forces recovered to baseline (Fig. 6k).

The feasibility study shows that we can insert EAs following the defined control strategy while keeping the exerted contact forces within safe levels. These findings are consistent with relevant studies [10], [20], [21] showing that robotic systems can reduce contact forces to safe levels. Also, the contacts forces in the Z-direction of our EA are generally lower than the forces presented in similar studies using robotic systems to insert commercially available EAs [10], [20]. It is relevant to mention that we used an unlubricated ST phantom to conduct our experiments, which potentially yielded higher contact forces due to friction. The size of our EA prototype, 3x scaled-up, may have also contributed to higher forces which we expect to see reduced in a real-size EA. These results will also have to be further investigated in temporal bones and *in vivo* to validate insertion contact forces and assess tissue trauma.
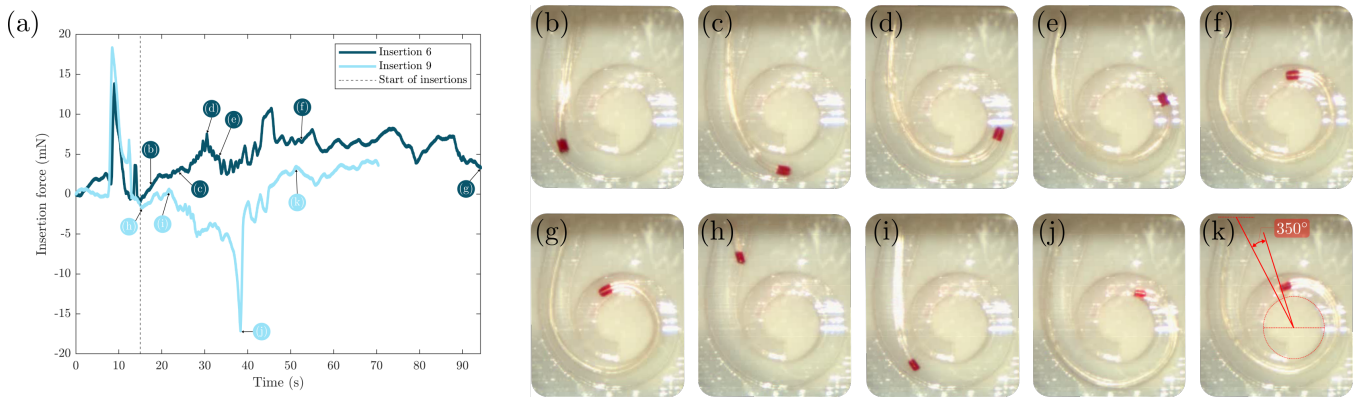
Fig. 6. (a) Force profile for insertions six and nine. Forces are negative in the insertion direction. Data is downsampled for better visualisation, and, as a result, peaks are softened compared to the complete data presented in Fig. 5. (b-k) Snapshots showing the self-shaping EA at the key points marked in force plots.

Other factors affecting the contact forces reported in this work are the control strategy implemented and the control over the EA temperature before insertion. Both need to be further improved and reevaluated in prototypes manufactured to scale. As mentioned in IV-A, temperature control can give the surgeon a longer time to place the robot at the desired approach angle (chosen pre-operatively) and avoid early curling of the EA before the first turn, as can be seen in Fig. 6h. Additionally, we will also have to explore different sensing approaches to retrieve the position of the EA within the cochlea in a clinically relevant way when line-of-sight approaches are not viable.

V. Conclusion

In this work, we have presented a teleoperated robotic system and a robotic vision approach to control the insertion of a self-shaping CI, providing the tools for a more delicate and atraumatic approach. We have shown that a well-tuned control approach can minimise instances of contact during insertion while achieving a successful insertion depth. The feasibility study has confirmed in a synthetic ST phantom that insertion contact forces are below the rupture threshold recorded in previous works while appropriate insertion depth can be achieved.

Acknowledgments

References

[1] F. Risi, "Considerations and Rationale for Cochlear Implant Electrode Design - Past , Present and Future," *The Journal of International Advanced Otology*, vol. 14, no. 3, pp. 382–391, 2018.

[2] C. James, K. Albegger, R. Battmer, S. Burdo, O. Deguine, N. Dillier, M. Gersdorff, R. Laszig, T. Lenarz, M. M. Rodriguez, N. R. Maci, O. Sterkers, E. V. O. N. Wallenberg, and B. Fraysse, "Preservation of residual hearing with cochlear implantation : How and why," *Acta Oto-Laryngologica*, vol. 125, pp. 481–491, 2005.

[3] MED-EL, "What is Residual Hearing?" pp. https://blog.medel.com/residual–hearing/, 2014.

[4] L. K. Holden, C. C. Finley, J. B. Firszt, T. A. Holden, C. Brenner, L. G. Potts, B. D. Gotter, S. S. Vanderhoof, K. Mispagel, G. Heydebrand, and M. W. Skinner, "Factors affecting open-set word recognition in adults with cochlear implants," *Ear and Hearing*, vol. 34, no. 3, pp. 342–360, 2013.

[5] A. Aschendorff, J. Kromeier, T. Klenzner, and R. Laszig, "Quality control after insertion of the nucleus contour and contour advance electrode in adults," *Ear and Hearing*, vol. 28, pp. 75S–79S, 4 2007.

[6] H. Ajieren, R. Reit, R. Lee, T. Pham, D. Shao, K. Lee, and W. Voit, "Robotic Insertion Aid for Self-Coiling Cochlear Implants," *MRS Advances*, vol. 1, no. 1, pp. 51–56, 2016.

[7] D. Bautista-Salinas, M. E. Abdelaziz, B. Temelkuran, E. M. Yeatman, C. T. Huins, and F. Rodriguez y Baena, "Towards a Functional Atraumatic Self-Shaping Cochlear Implant," *Macromolecular Materials and Engineering*, vol. 307, no. 1, pp. 1–9, 2022.

[8] B. P. O'Connell, J. B. Hunter, and G. B. Wanna, "The importance of electrode location in cochlear implantation," *Laryngoscope Investigative Otolaryngology*, vol. 1, no. 6, pp. 169–174, 2016.

[9] S. Weber, K. Gavaghan, W. Wimmer, T. Williamson, N. Gerber, J. Anso, B. Bell, A. Feldmann, C. Rathgeb, M. Matulic, M. Stebinger, D. Schneider, G. Mantokoudis, O. Scheidegger, F. Wagner, M. Kompis, and M. Caversaccio, "Instrument flight to the inner ear," *Science Robotics*, vol. 2, no. 4, p. eaal4916, 2017.

[10] J. Pile and N. Simaan, "Modeling, design, and evaluation of a parallel robot for cochlear implant surgery," *IEEE/ASME Transactions on Mechatronics*, vol. 19, no. 6, pp. 1746–1755, 2014.

[11] A. Hussong, T. S. Rau, T. Ortmaier, B. Heimann, T. Lenarz, and O. Majdani, "An automated insertion tool for cochlear implants: Another step towards atraumatic cochlear implant surgery," *International Journal of Computer Assisted Radiology and Surgery*, vol. 5, no. 2, pp. 163–171, 2010.

[12] G. Z. Yang, J. Cambias, K. Cleary, E. Daimler, J. Drake, P. E. Dupont, N. Hata, P. Kazanzides, S. Martel, R. V. Patel, V. J. Santos, and R. H. Taylor, "Medical robotics-Regulatory, ethical, and legal considerations for increasing levels of autonomy," *Science Robotics*, vol. 2, no. 4, pp. 2–4, 2017.

[13] P. Aebischer, G. Mantokoudis, S. Weder, L. Anschuetz, M. Caversaccio, and W. Wimmer, "In-Vitro Study of Speed and Alignment Angle in Cochlear Implant Electrode Array Insertions," *IEEE Transactions on Biomedical Engineering*, vol. 69, no. 1, pp. 129–137, 2022.

[14] M. G. Zuniga, S. Hügl, B. G. Engst, T. Lenarz, and T. S. Rau, "The Effect of Ultra-slow Velocities on Insertion Forces: A Study Using a Highly Flexible Straight Electrode Array," *Otology and Neurotology*, vol. 42, no. 8, pp. E1013–E1021, 2021.

[15] G. Kontorinis, T. Lenarz, T. Stöver, and G. Paasche, "Impact of the insertion speed of cochlear implant electrodes on the insertion forces." *Otology & Neurotology*, vol. 32, no. 4, pp. 565–70, 2011.

[16] G. Bradski, "The OpenCV Library," *Dr. Dobb's Journal of Software Tools*, 2000.

[17] T. Stöver, P. Issing, G. Graurock, P. Erfurt, Y. ElBeltagy, G. Paasche,

and T. Lenarz, "Evaluation of the Advance Off-Stylet insertion technique and the cochlear insertion tool in temporal bones," *Otology and Neurotology*, vol. 26, no. 6, pp. 1161–1170, 2005.

[18] J. R. Clark, F. M. Warren, and J. J. Abbott, "A Scalable Model for Human Scala-Tympani Phantoms," *Journal of Medical Devices*, vol. 5, no. 1, p. 014501, 2011.

[19] T. S. Rau, T. Ehmann, M. G. Zuniga, K. Plaskonka, A. Keck, O. Majdani, and T. Lenarz, "Toward a cochlear implant electrode array with shape memory effect for post-insertion perimodiolar positioning," *Journal of Biomedical Materials Research - Part B Applied Biomaterials*, pp. 1–12, 2022.

[20] J.-P. Kobler, D. Beckmann, T. S. Rau, O. Majdani, and T. Ortmaier, "An automated insertion tool for cochlear implants with integrated force sensing capability," *International Journal of Computer Assisted Radiology and Surgery*, vol. 9, pp. 481–494, 2014.

[21] A. N. Vadivelu, Z. Liu, D. S. Gunawardena, B. Chen, H. Y. Tam, S. O'Leary, and D. Oetomo, "Integrated Force Sensor in a Cochlear Implant for Hearing Preservation Surgery," *Proceedings of the Annual International Conference of the IEEE Engineering in Medicine and Biology Society, EMBS*, pp. 3819–3822, 2019.